Supporting Information

Mechanisms for improved high-speed processability of active layer materials in bulk-heterojunction organic photovoltaics

Table-of-contents

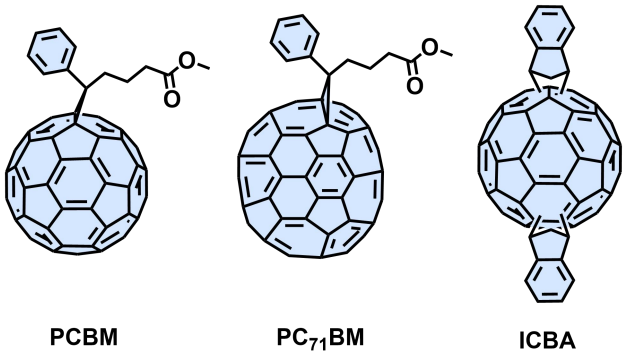

Supplementary Fig. 1. Chemical structures of PCBM series acceptors (PCBM[1], $PC_{71}BM$[2] and ICBA[3]) investigated in this work.

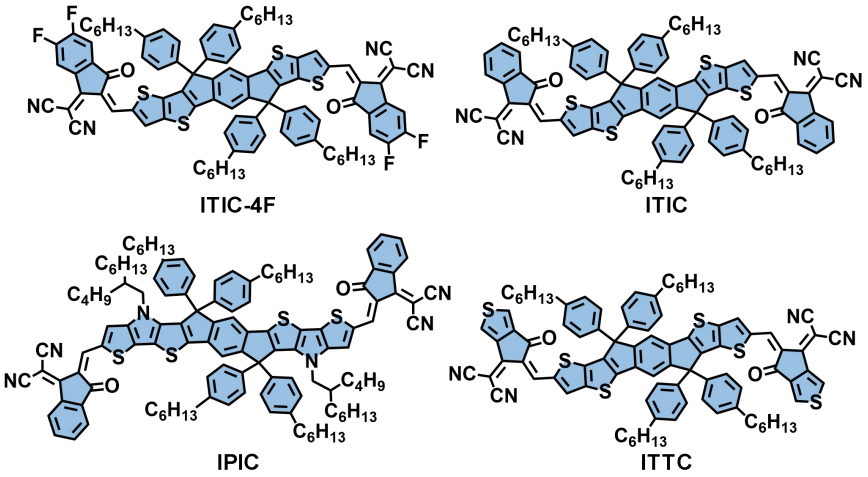

Supplementary Fig. 2. Chemical structures of ITIC series acceptors (ITIC-4F[4], ITIC[5], IPIC[6] and ITTC[7]) investigated in this work.

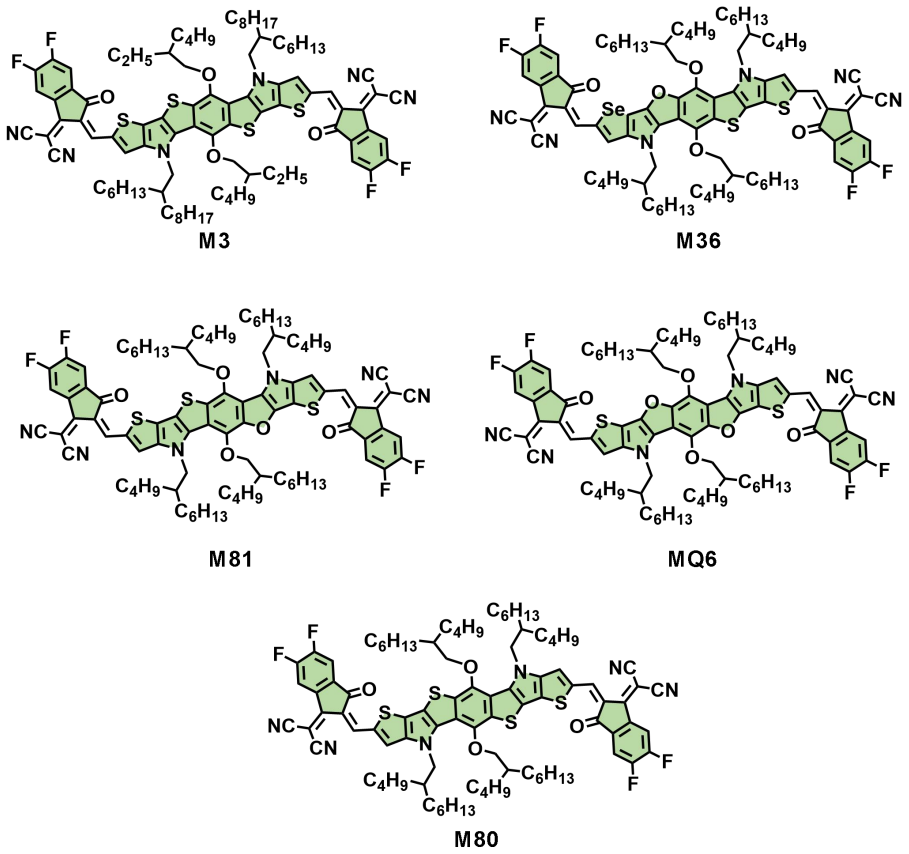

Supplementary Fig. 3. Chemical structures of M3 series acceptors (M3[8], M36[9], M81[9], MQ6[10] and M80[9]) investigated in this work.

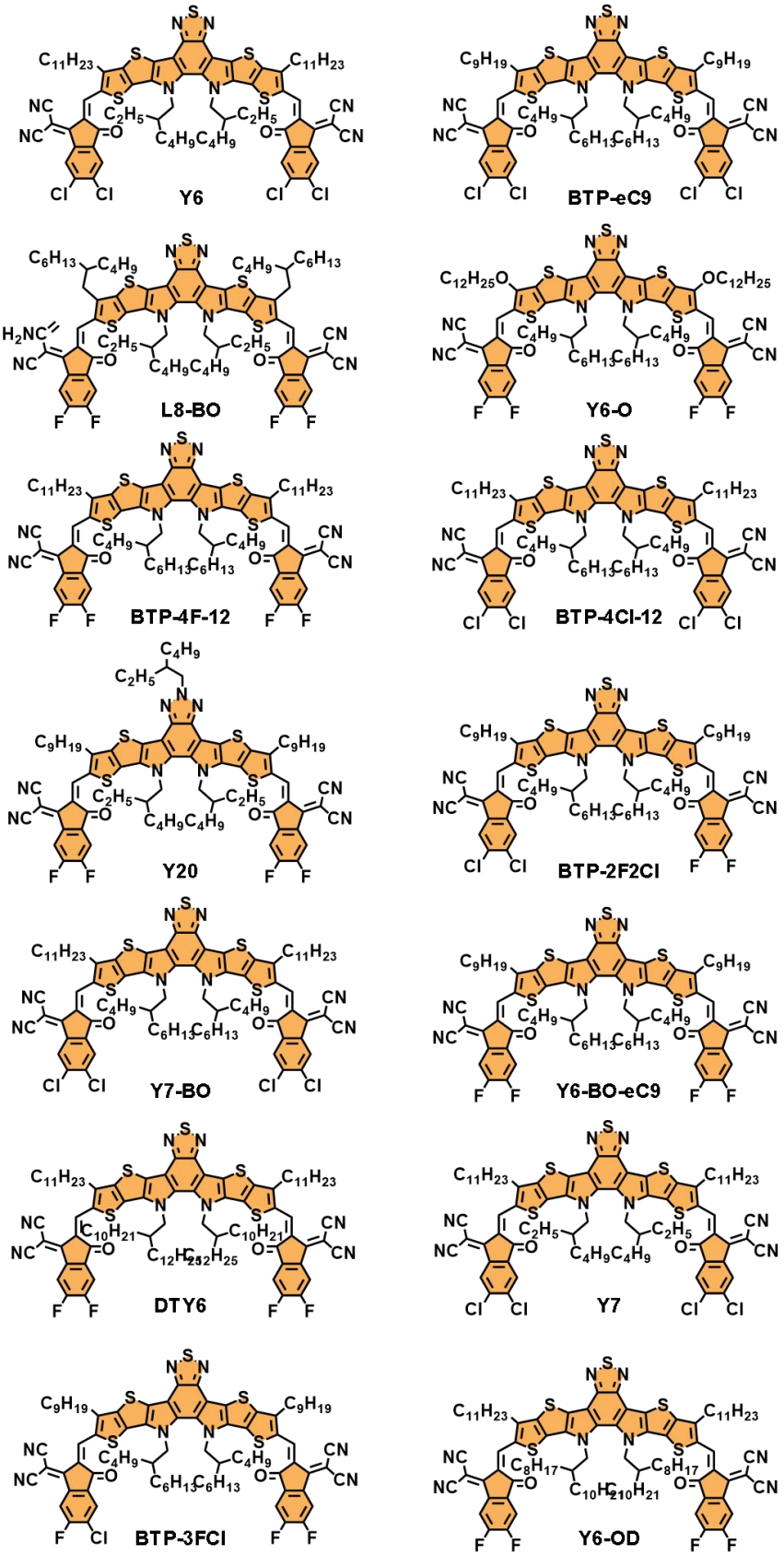

Supplementary Fig. 4. Chemical structures of Y6 series acceptors (Y6[11], BTP-eC9[12], L8-BO[13], Y6-O[14], BTP-4Cl-12[15], Y20[16], BTP-2F2Cl[17], Y7-BO[18], Y6-BO-eC9[19], DTY6[20], Y7[21], BTP-3FCl and Y6-OD[22]) investigated in this work.

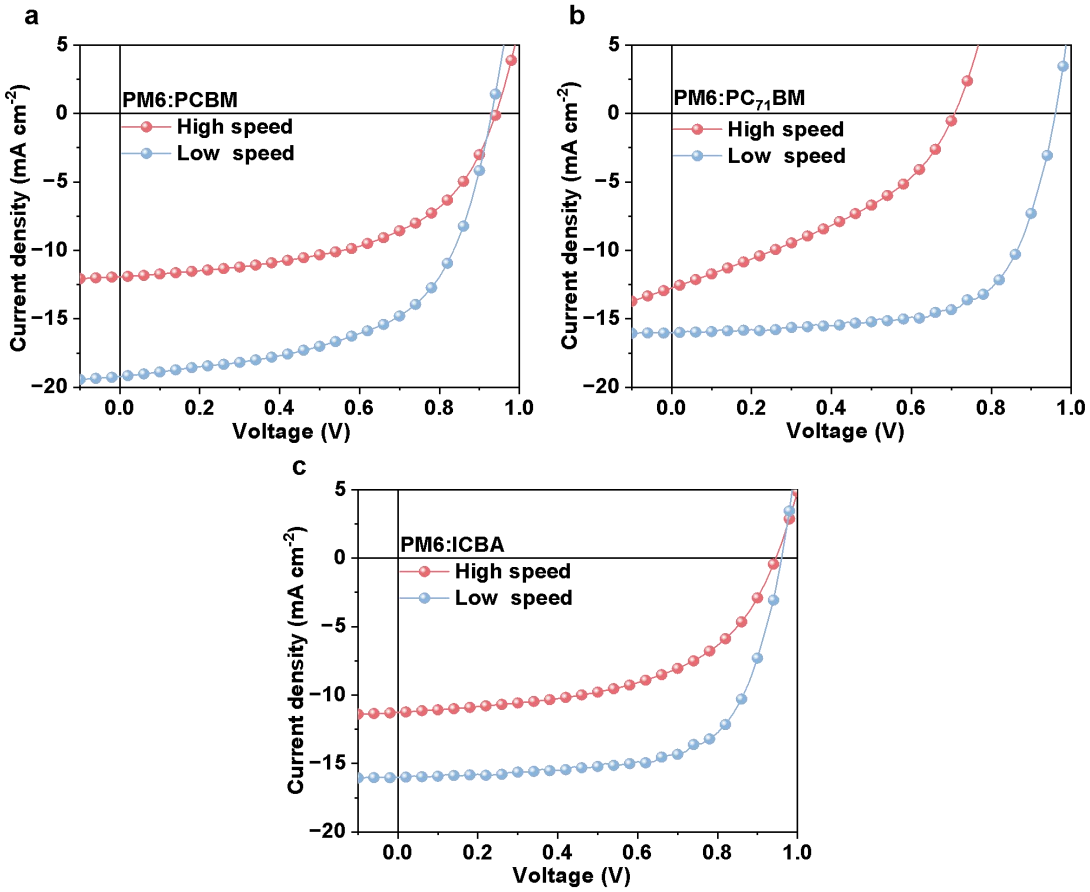

Supplementary Fig. 5. *J-V* curves of the devices composed of PM6 as the donor and PCBM series as the acceptor fabricated by low-speed and high-speed coating processes.

Supplementary Table 1. Summary of the PCE of the device of PM6:PCBM series acceptors fabricated under normal speed and high speed.

Acceptor	Speed (m min^{-1})	V_{OC} (V)	J_{SC} (mA cm^{-2})	FF (%)	PCE[a] (%)
PCBM		0.930	19.22	57.99	10.37 (9.81±0.56)
ICBM	1.8	0.960	16.03	66.94	10.30 (10.22±0.08)
$PC_{71}BM$		0.916	12.70	47.60	5.54 (5.12±0.42)
PCBM		0.941	11.93	53.42	6.00 (5.53±0.47)
ICBM	30.0	0.970	14.77	34.90	5.00 (4.33±0.67)
$PC_{71}BM$		0.708	12.74	37.31	3.37 (3.15±0.22)

[a)]The average PCE values with standard deviations were obtained from 10 independent cells.

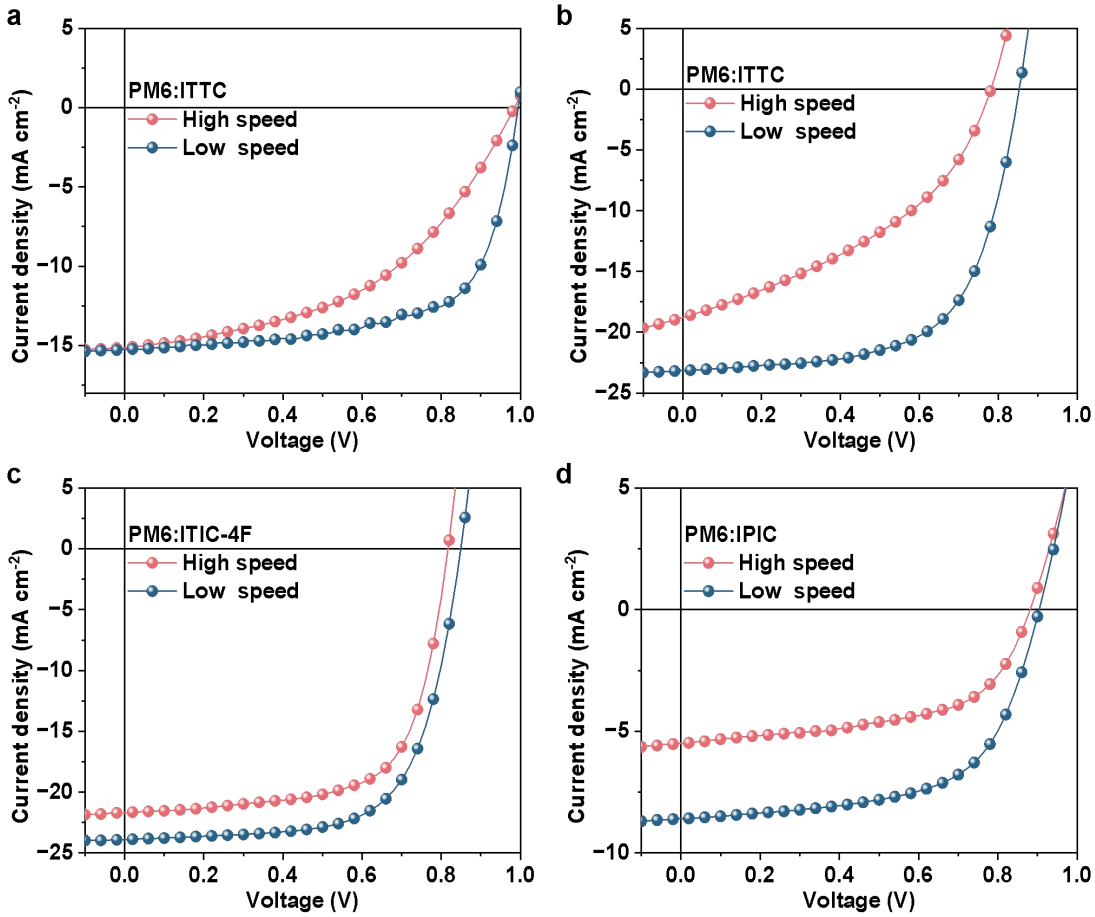

Supplementary Fig. 6. *J-V* curves of the devices composed of PM6 as the donor and ITIC series as the acceptor fabricated by low-speed and high-speed coating processes.

Supplementary Table 2. Summary of the PCE of the device of PM6:ITIC series acceptors fabricated under normal speed and high speed.

Acceptor	Speed (m min^{-1})	V_{OC} (V)	J_{SC} (mA cm^{-2})	FF (%)	PCE[a] (%)
IT-4F	1.8	0.849	23.89	66.83	13.56 (13.1±0.46)
ITIC		0.994	15.24	66.28	10.04 (9.86±0.18)
IPIC		0.994	8.60	61.09	4.75 (4.49±0.26)
ITTC		0.853	23.16	63.18	12.48 (11.86±0.61)
IT-4F	30.0	0.817	21.67	67.08	11.88 (11.48±0.40)
ITIC		0.985	15.14	46.85	6.99 (6.96±0.03)
IPIC		0.881	5.50	56.71	2.75 (2.50±0.25)
ITTC		0.782	18.78	40.22	5.90 (5.22±0.68)

[a)]The average PCE values with standard deviations were obtained from 10 independent cells.

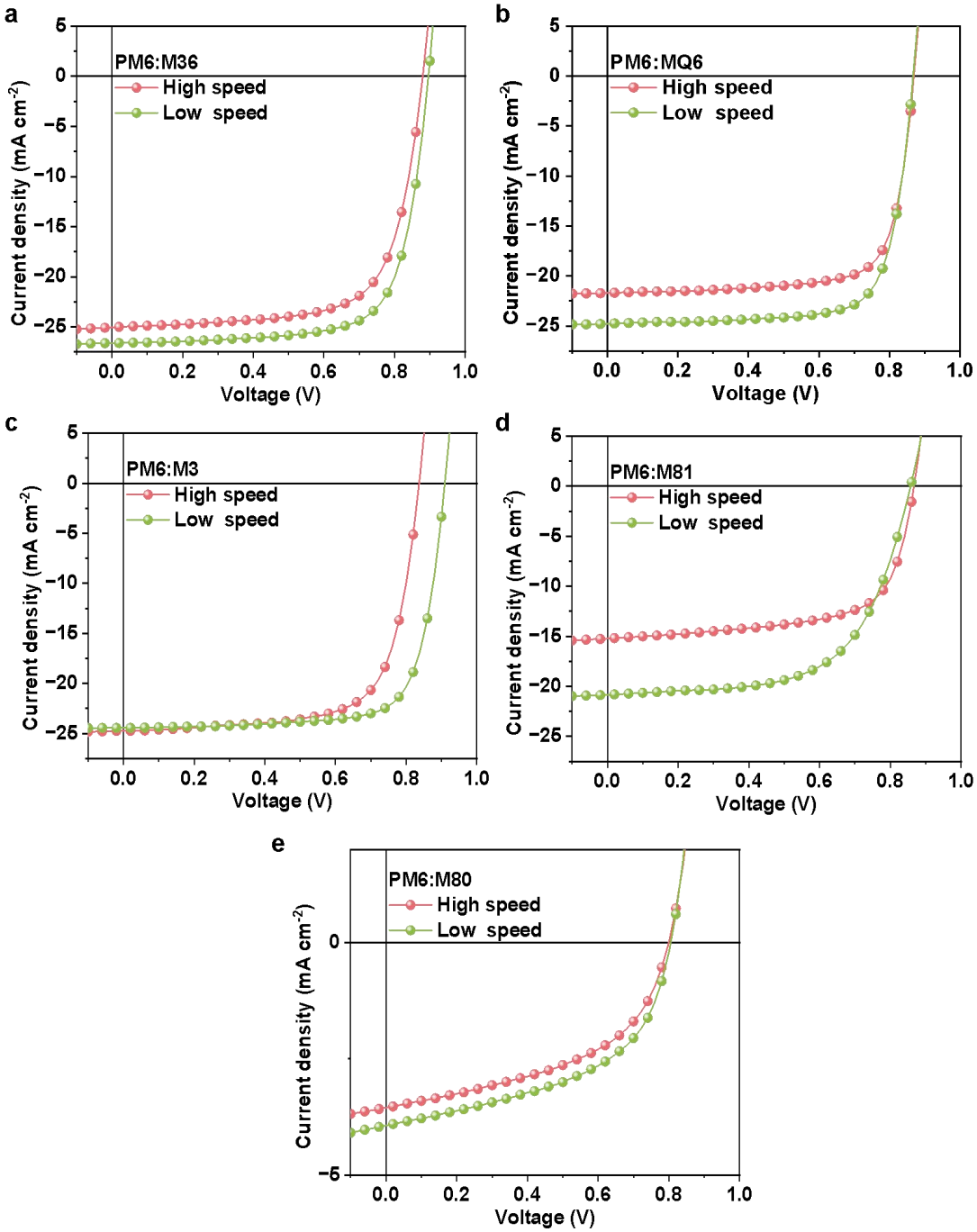

Supplementary Fig. 7. *J-V* curves of the devices composed of PM6 as the donor and M3 series as the acceptor fabricated by low-speed and high-speed coating processes.

Supplementary Table 3. Summary of the PCE of the device of PM6:M3 series acceptors fabricated under normal speed and high speed.

Acceptor	Speed (m min^{-1})	V_{OC} (V)	J_{SC} (mA cm^{-2})	FF (%)	PCE[a] (%)
M3		0.909	24.44	75.29	16.73 (16.26±0.47)
M36		0.896	26.60	72.70	17.32 (16.64±0.68)
M80	1.8	0.805	3.94	50.16	1.59 (1.37±0.22)
M81		0.857	20.85	61.19	10.93 (10.59±0.34)
MQ6		0.867	24.78	75.13	16.14 (16.00±0.13)
M3		0.837	24.74	70.15	14.52 (14.37±0.15)
M36		0.880	25.04	69.67	15.34 (14.71±0.63)
M80	30.0	0.800	3.55	48.53	1.38 (0.84±0.54)
M81		0.867	15.23	65.92	8.70 (8.59±0.11)
MQ6		0.869	21.70	74.98	14.14 (13.79±0.35)

[a)]The average PCE values with standard deviations were obtained from 10 independent cells.

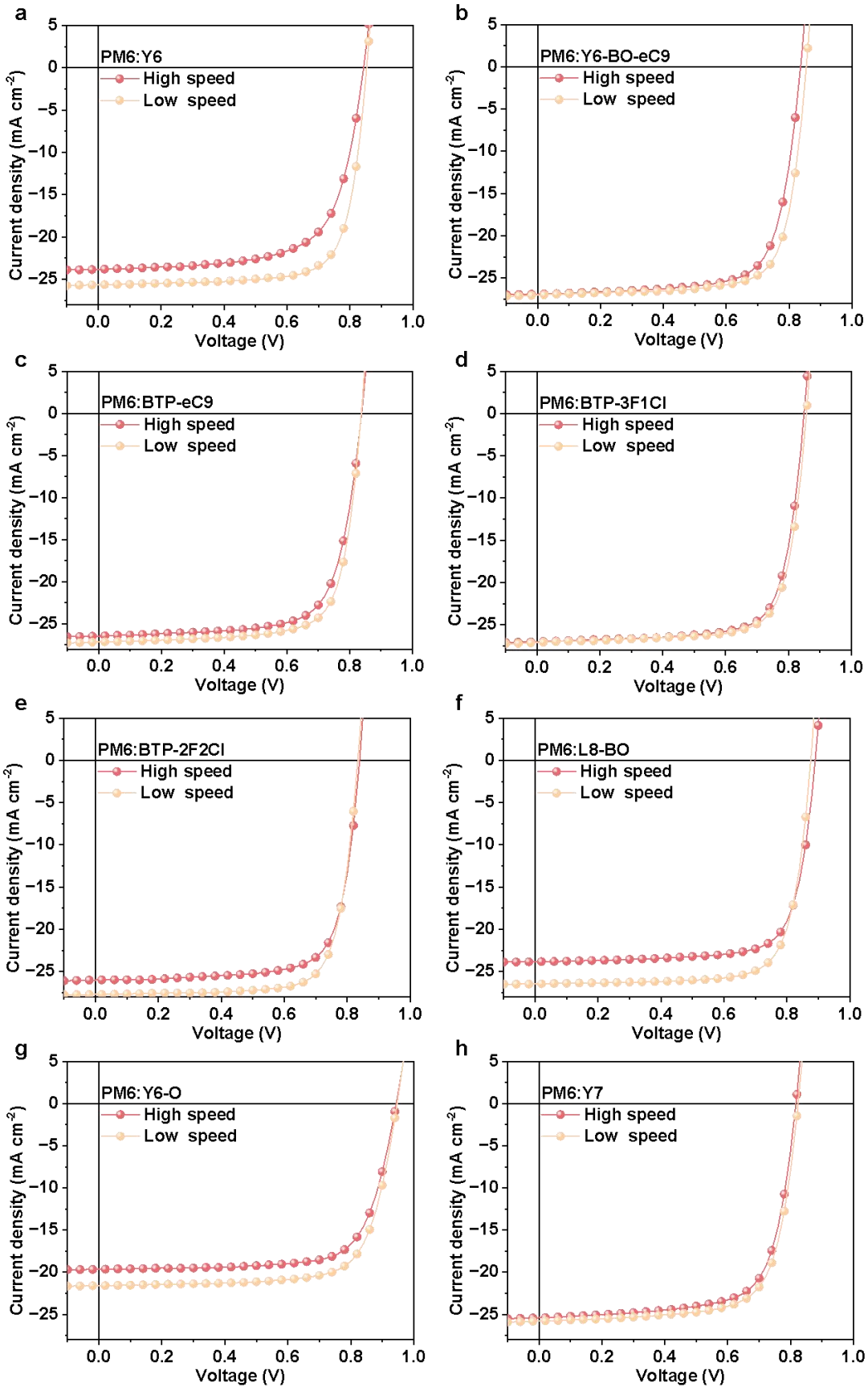
a
PM6:Y6
High speed
Low speed
b
PM6:Y6-BO-eC9
High speed
Low speed
c
PM6:BTP-eC9
High speed
Low speed
d
PM6:BTP-3F1Cl
High speed
Low speed
e
PM6:BTP-2F2Cl
High speed
Low speed
f
PM6:L8-BO
High speed
Low speed
g
PM6:Y6-O
High speed
Low speed
h
PM6:Y7
High speed
Low speed
Current density (mA cm^{-2})
Voltage (V)
5
0
−5
−10
−15
−20
−25
0.0
0.2
0.4
0.6
0.8
1.0

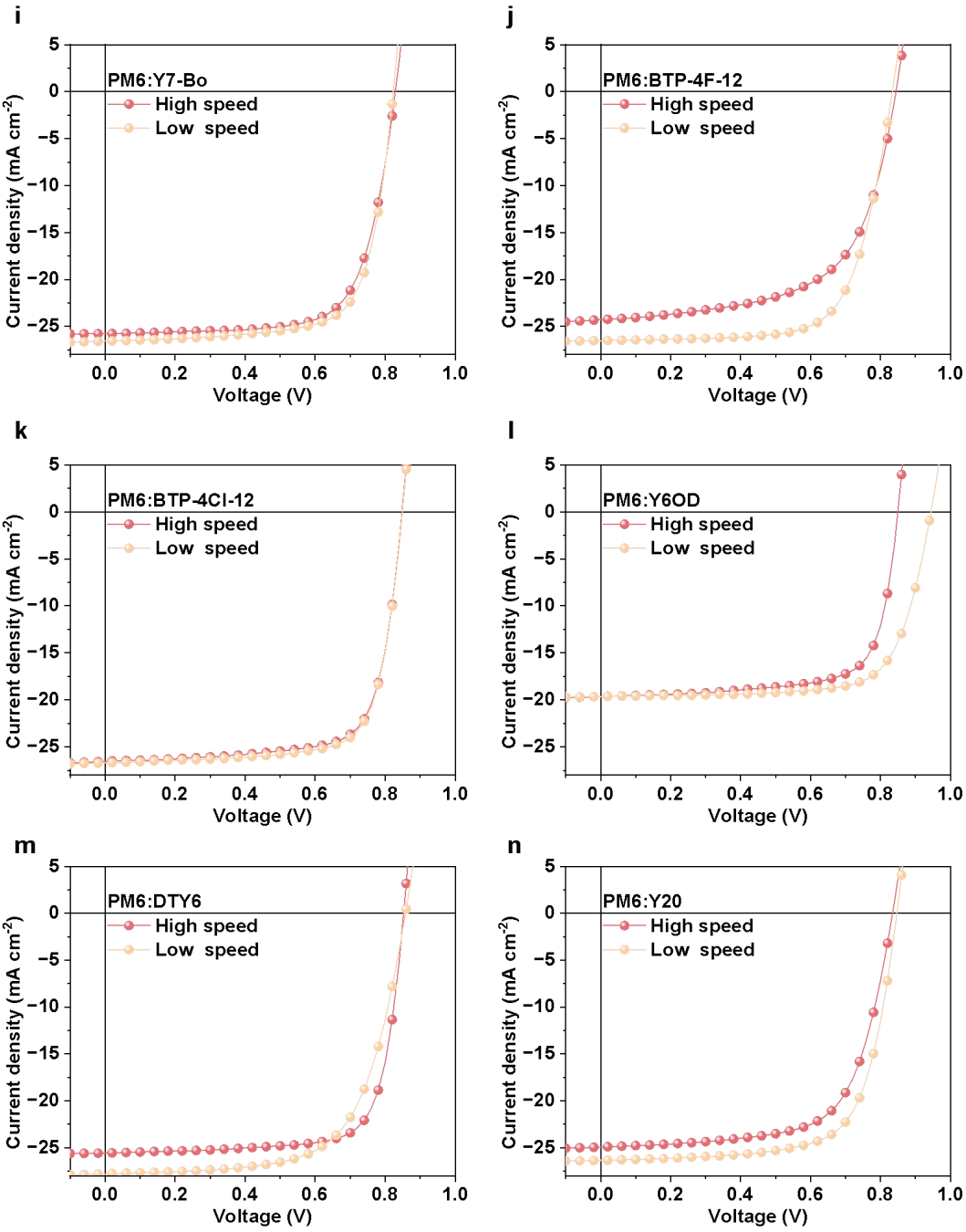

Supplementary Fig. 8. *J-V* curves of the devices composed of PM6 as the donor and Y6 series as the acceptor and fabricated by low-speed and high-speed coating processes.

Supplementary Table 4. Summary of the PCE of the device of PM6:Y6 series acceptors fabricated under normal speed and high speed.

Acceptor	Speed (m min^{-1})	V_{OC} (V)	J_{SC} (mA cm^{-2})	FF (%)	PCE[a] (%)
Y6	1.8	0.853	25.63	75.59	16.53 (16.34±0.09)
Y6-BO-eC9		0.855	27.02	75.37	17.41 (16.82±0.59)
BTP-eC9		0.850	27.29	76.24	17.69 (17.55±0.14)
BTP-3F1Cl		0.858	27.11	75.64	17.59 (17.25±0.34)
BTP-2F2Cl		0.837	27.15	74.80	17.23 (17.11±0.12)
L8-BO		0.876	26.47	76.46	17.72 (17.53±0.19)
Y6-O		0.947	21.58	73.49	15.02 (14.81±0.21)
Y7		0.824	25.78	72.14	15.32 (14.69±0.63)
Y7-BO		0.823	26.56	72.26	15.80 (15.16±0.64)
BTP-4F-12		0.834	26.51	69.82	15.43 (15.27±0.16)
BTP-4Cl-12		0.849	26.69	74.13	16.80 (16.75±0.05)
Y6-OD		0.865	23.58	74.15	15.12 (14.65±0.47)
DTY6		0.852	25.57	75.59	16.48 (16.22±0.26)
Y20		0.847	26.36	70.19	15.66 (15.29±0.37)
Y6	30.0	0.843	23.83	67.99	13.65 (13.43±0.12)
Y6-BO-eC9		0.837	26.90	73.19	16.47 (16.16±0.31)
BTP-eC9		0.851	27.84	73.51	17.41 (17.13±0.28)
BTP-3F1Cl		0.850	27.00	75.01	17.21 (16.77±0.43)
BTP-2F2Cl		0.838	26.44	72.06	15.96 (15.89±0.06)
L8-BO		0.890	23.84	75.72	16.06 (15.72±0.34)
Y6-O		0.944	19.65	72.88	13.52 (13.19±0.33)
Y7		0.817	25.39	70.85	14.69 (14.45±0.24)
Y7-BO		0.829	25.77	71.05	15.18 (15.04±0.13)
BTP-4F-12		0.844	24.28	60.95	12.49 (12.41±0.08)
BTP-4Cl-12		0.848	26.54	73.66	16.57 (16.18±0.39)
Y6-OD		0.849	19.65	72.77	12.15 (11.94±0.21)
DTY6		0.858	27.79	65.55	15.63 (15.15±0.48)
Y20		0.834	24.93	66.82	13.9 (13.84±0.06)

[a)]The average PCE values with standard deviations were obtained from 10 independent cells.

Supplementary Table 5. Full names of acceptor material and corresponding code names and A_h value.

Acceptor	Mark	A_h	Average A_h
PCBM series			
PCBM	S-F1	0.578	0.510
ICBA	S-F2	0.475	
$PC_{71}BM$	S-F3	0.478	
ITIC series			
IT-4F	S-T1	0.742	0.654
ITIC	S-T2	0.696	
IPIC	S-T3	0.579	
ITTC	S-T4	0.599	
M3 series			
M3	S-M1	0.868	0.859
M36	S-M2	0.886	
M80	S-M3	0.867	
M81	S-M4	0.796	
MQ6	S-M5	0.876	
Y6 series			
Y6	S-Y1	0.845	0.917
Y6-BO-eC9	S-Y2	0.946	
BTP-eC9	S-Y3	0.984	
BTP-3F1Cl	S-Y4	0.979	
BTP-2F2Cl	S-Y5	0.926	
L8-BO	S-Y6	0.906	
Y6-O	S-Y7	0.900	
Y7	S-Y8	0.959	
Y7-BO	S-Y9	0.961	
BTP-4F-12	S-Y10	0.809	
BTP-4Cl-12	S-Y11	0.986	
Y6-OD	S-Y12	0.804	
DTY6	S-Y13	0.948	
Y20	S-Y14	0.888	

Supplementary Note 1.

Simulation of fluid flow within the meniscus at various printing speeds:

A two-dimensional model was built using COMSOL Multiphysics to simulate the fluid flow in the coating blade under two different coating speeds (1.8 m min^{-1} and 30 m min^{-1}). The solution was swept out by sheer force under the blade, and the movement of the substrate drove the flow of the solution. Considering computing power constraints and grid density. In this study, we only research the effect of coating speed on fluid flow distribution. Geometric parameters of blade edge in the model are measured from real blade used in this research, as shown in **Supplementary Table 6**.

Multiphase material including air and coating solution was used for flow calculation. The two-phase flow field driven by airflow physical and Laminar flow physical fields were used to simulate fluid flow.

In the laminar physical field, the fluid was modeled using the Navier-Stokes equations and was described as an incompressible Newtonian fluid as follows:

$$\rho\left[\frac{\partial u}{\partial t}+(u\cdot\nabla)u\right]=-\nabla p+\nabla\cdot(\mu\nabla u)+\mathrm{F}$$

$$\rho\nabla\cdot u=0$$

where ρ is the liquid density, u is the velocity vector, p is the pressure, μ is the viscosity, and F is the body force.

In the two-phase flow physical field, the evolution of phase boundary was modeled using the fluid dynamics and stresses formulas in a multi-phase system as follows:

$$F_{St}=\frac{2}{\rho_1+\rho_2}\left(\rho_1 H\left(\frac{V_{f,1}-0.5}{d_{s,F_{St}}}\right)+\rho_2 H\left(\frac{V_{f,2}-0.5}{d_{s,F_{St}}}\right)\right)\left(\frac{\lambda}{\epsilon_{pf}^2}\psi-\frac{\partial f}{\partial\phi}\right)\nabla$$

$$V_{f,1}=\frac{1-\phi}{2},\ V_{f,2}=\frac{1+\phi}{2},V_{f,1}+V_{f,2}=1$$

where F_{st} is the stress or force, ρ_1 and ρ_2 are the density of two flows, $V_{f,1}$ and $V_{f,2}$ are relevant volume fractions, the H function typically denotes a Heaviside step function, $d_{s,\,Fst}$ is the characteristic dimension defied by the index flow property, Φ is the stress

or displacement gradient between two flows, ϵ_{pf} is a squared parameter related to permittivity or porosity, λ describes the interaction strength between different phases or components in the material.

As illustrated in **Supplementary Fig. 9**, the edge of the blade head and baseplate were set as the wetted wall. The black line were set as inlet and open boundary, respectively. To apply a sheer force on the solution, the green line was set as a Navier slip wall with a slip speed that was equal to the coating speed. The place with a blue color shadow was filled by coating fluid in the initial condition. Simulation results were obtained by the combination of phase initialization and time-dependent study. The fluid flow at different printing speeds was calculated by parametric sweep. To emphasize the formation process of the wet film, the observation range was set in the blue dot line area. Corresponding press gradient data were extracted to highlight the most predominant wet film formation behavior.

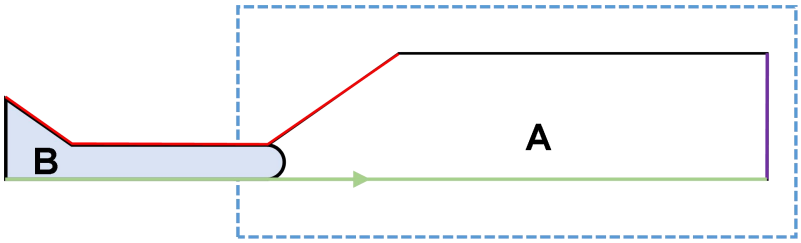

Supplementary Fig. 9. The wall and study regime in the simulation model.

Supplementary Table 6. The geometric parameters of the simulation model.

Parameter	Value	Description
G	0.4 mm	Blade gap
W	4 mm	Blade width
E_u	45°	Upstream die angle
E_d	45°	Downstream die angle
L_u	5 mm	Upstream length
L_d	5 mm	Downstream length
S_blade	0.03/5 m s^{-1}	Coating speed
S_in	0.03/5 m s^{-1}	Inlet speed

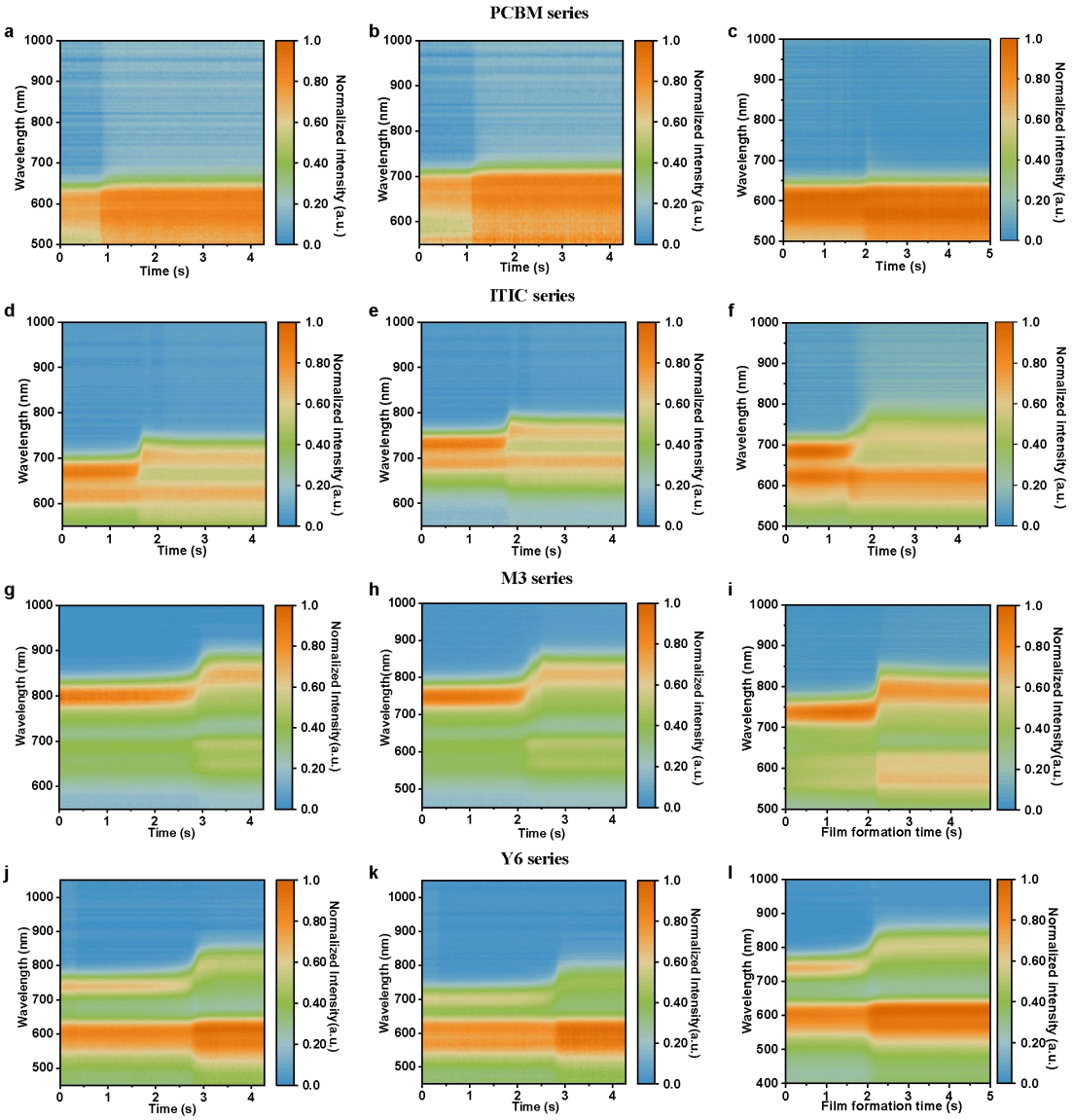

Supplementary Fig. 10. *In-situ* ultraviolet-visible (UV-vis) spectrum of blends of PM6:SMAs, the codes of acceptors were (a) S-F1, (b) S-F2, (c) S-F3, (d) S-T1, (e) S-T2, (f) S-T4, (g) S-M2, (h) S-M4, (i) S-M4, (j) S-Y6, (k) S-Y7 and (l) S-Y9, respectively.

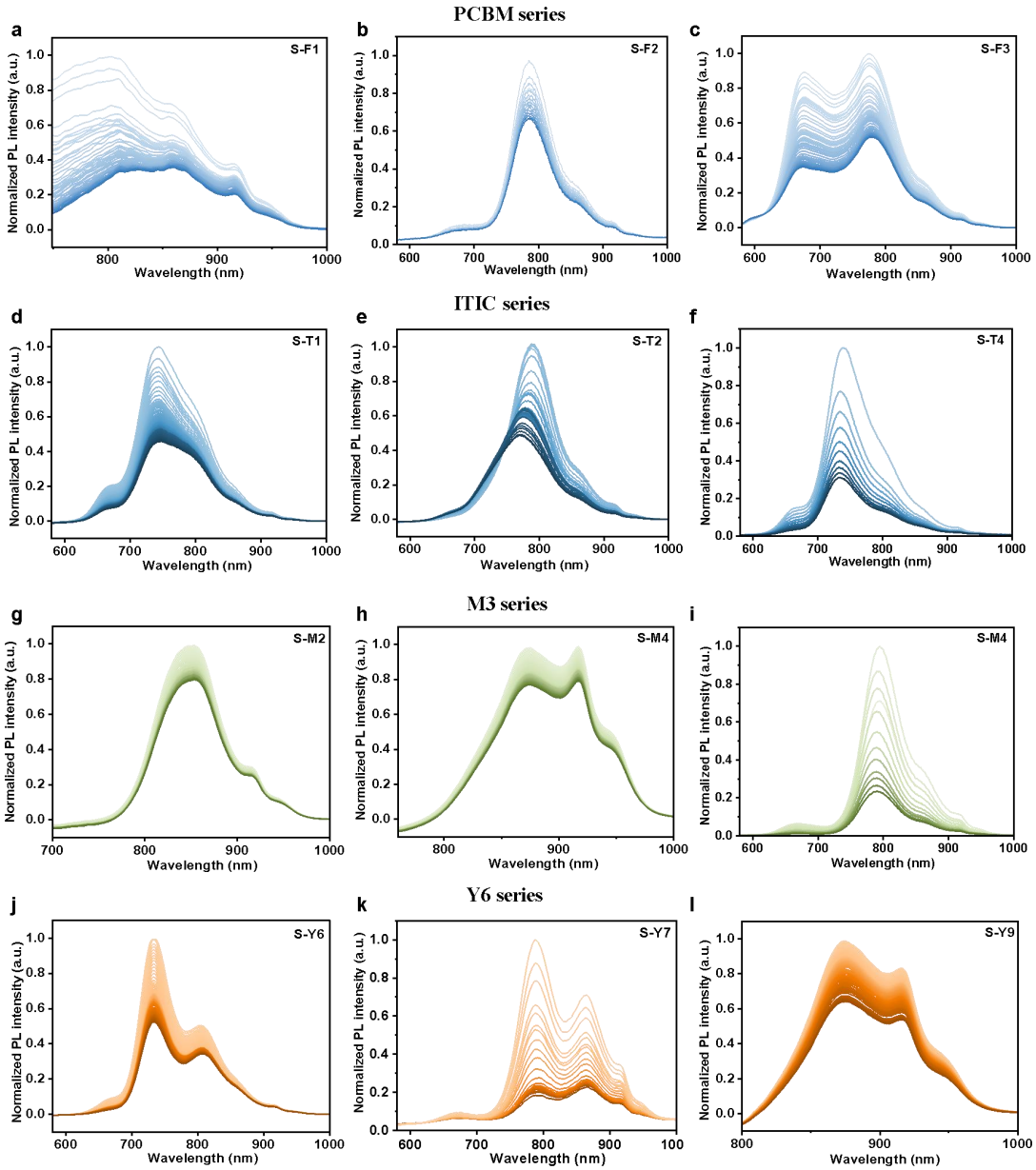

Supplementary Fig.11. *In-situ* photoluminescence (PL) spectrum of blends of PM6:SMAs, the codes of acceptors were (a) S-F1, (b) S-F2, (c) S-F3, (d) S-T1, (e) S-T2, (f) S-T4, (g) S-M2, (h) S-M4, (i) S-M4, (j) S-Y6, (k) S-Y7 and (l) S-Y9, respectively.

Supplementary Table 7. The HSP value of pure solvents and blends. The codes b-CH, b-CM, and b-CP mean the blends of chloroform and n-hexane, chloroform and methanol, chloroform, and propylene carbonate, respectively. The number behind the code means the percentage of poor solvent in blends, for example, b-CM7 means blend consisting of 30% chloroform and 70% methanol. HSP values of chloroform, *n*-hexane, methanol, and propylene carbonate are provided by the standard solvents' HSP list, while the HSP values of blends were calculated according to the linear rule.

Solvents	Dispersive ($MPa^{1/2}$)	Polar ($MPa^{1/2}$)	H-bond ($MPa^{1/2}$)
chloroform	17.8	3.1	5.7
n-Hexane	14.9	0	0
methanol	14.7	12.3	22.3
propylene carbonate	20	18	4.1
b-CH1	17.51	2.79	5.13
b-CH2	17.22	2.48	4.56
b-CH3	16.93	2.17	3.99
b-CH4	16.64	1.86	3.42
b-CH5	16.35	1.55	2.85
b-CH6	16.06	1.24	2.28
b-CH7	15.77	0.93	1.71
b-CH8	15.48	0.62	1.14
b-CH9	15.19	0.31	0.57
b-CM1	17.49	4.02	7.36
b-CM2	17.18	4.94	9.02
b-CM3	16.87	5.86	10.68
b-CM4	16.56	6.78	12.34
b-CM5	16.25	7.7	14
b-CM6	15.94	8.62	15.66
b-CM7	15.63	9.54	17.32
b-CM8	15.32	10.46	18.98
b-CM9	15.01	11.38	20.64
b-CP1	18.02	4.59	5.54
b-CP2	18.24	6.08	5.38
b-CP3	18.46	7.57	5.22
b-CP4	18.68	9.06	5.06
b-CP5	18.9	10.55	4.9
b-CP6	19.12	12.04	4.74
b-CP7	19.34	13.53	4.58
b-CP8	19.56	15.02	4.42
b-CP9	19.78	16.51	4.26

Supplementary Table 8. The HSP value of pure solvents and binary solvent.

Acceptor	Dispersive ($MPa^{1/2}$)	Polar ($MPa^{1/2}$)	H-bond ($MPa^{1/2}$)	R_0 ($MPa^{1/2}$)	D_{SA} ($MPa^{1/2}$)	D_{AD} ($MPa^{1/2}$)	P_{dc} ($\times10^{-2}$)
S-F1	17.04	4.96	7.89	4.9	3.68	5.83	-3.33
S-F2	16.49	4.41	7.82	5.1	4.00	6.27	-5.42
S-F3	16.77	4.7	8.08	4.8	3.96	6.20	-8.07
S-T1	16.74	3.87	7.07	4.2	2.99	5.32	-0.55
S-T2	16.49	4.41	7.82	4.5	4.00	6.27	-11.78
S-T3	16.75	4.29	7.53	5.4	3.43	5.71	5.59
S-M3	16.98	5.23	7.01	5.6	3.30	5.25	10.18
S-M4	16.4	3.62	6.49	4.9	3.17	5.36	4.64
S-M5	16.68	3.51	5.22	4.1	2.28	4.13	13.85
S-Y3	17.4	4.99	4.17	5	2.25	2.76	39.50
S-Y10	17.3	5.17	5.87	5.02	2.42	4.02	23.78
S-Y15	17.2	4.1	4.73	4.4	1.61	3.05	44.47

Note: Dispersive, Polar, H-bond are the dispersive force, polar force and H-bond force component of cohesion energy, respectively. R_0 is the radius of solute sphere, D_{SA} is the HSP space distance between the solvent and acceptor, D_{AD} is the HSP space distance between the donor and acceptor, P_{dc} is defined as the priority of donor crystallization during the film formation process.

Supplementary Note 2.

Hansen Solubility Parameters:

Gradient measurement[23] was employed to determine the HSP (Hansen Solubility Parameters) point coordinates (H-bond, Polar, Dispersive components) and the radius of the solubility sphere. We utilized three groups of good solvent-poor solvent blends as test solvents (Chloroform: n-Hexane, Chloroform: Methanol, and Chloroform: Propylene Carbonate). Each group consisted of 9 mixed solvents, starting from pure chloroform, with the poor solvent gradually introduced at 10% volume fraction increments, until the poor solvent reached 90% of the total volume. The HSP points of the resulting mixed solvents will follow a linear rule in HSP space, forming a claw-like pattern. The target acceptor material is soluble in chloroform, and by scanning in three distinct directions in HSP space, the solubility radius, and center can be determined with greater precision than typically achieved with conventional solvent mixtures. Considering the minimum concentration of dilute solutions suitable for high-speed processing is typically around 5 mg mL^{-1}, we used this value as the threshold to define "soluble" and "poorly soluble" states.

***Donor-acceptor-solvent triangle model and Calculation of P_{dc} Value*:**

In this article, an HSP model was established to calculate the donor-acceptor-solvent triangle relationship and corresponding crystal behavior during the crystallization stage in film formation process. The corresponding module illustration and parameters are listed below.

Supplementary Table 9. The parameters list of HSP triangle model.

Parameter	Description
P_{dc}	The priority of donor crystallization
R_0	The solute sphere radius of the solute
D_{DA}	The HSP space distance between the donor and acceptor
D_{SA}/ D_{SD}	The HSP space distance between solvent and acceptor/ donor
R_A/ R_D	The solute sphere radius of the acceptor/ donor
RED_A / RED_D	The relative energy differences of the acceptor/ donor

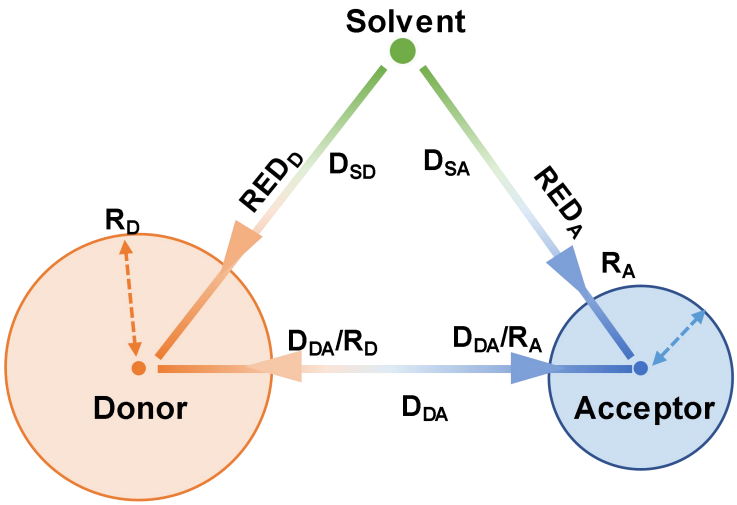

$$P_{dc} = (RED_D - RED_A)/((D_{DA}/R_D + D_{DA}/R_A)/(\frac{1}{2}))$$
$$= (RED_D - RED_A)\,(H(R_D, R_A)D_{DA})$$
$$= (R_{SA}R_D - R_{SD}R_A)/(R_{DA}\,\overline{(R_D, R_A)})$$

Supplementary Fig. 12. The D-A-solvent triangle and the corresponding parameters.

According to formula $Difference^2 = 2.046^2(\delta D_A - \delta D_B)^2 + (\delta P_A - \delta P_B)^2 + (\delta H_A - \delta H_B)^2$ given in the HSP guidebook, each solute/solvent can be determined as a point in the HSP 3D space, in this work, we define their point position as a vector *Px*, and the difference between two solutes can regarded as Euclidean distance between two vectors. For the solute point, as the set of boundary concentration, a soluble edge was attached to the solute in HSP space, the solute point was transformed into the solute sphere, and the radius of the sphere was used to measure the solute's inclusiveness to the solute. For a certain kind of solvent, we used the RED value (The solute-solvent point distance divided by the solute sphere radius) to compare the crystallization priority of different acceptors in the same solvents. By extension, the miscibility behavior of the donor and acceptor was accounted for by the solute-solvent point distance divided by the solute sphere radius. The explanation above can be summarized in the formula below:

$$P_X = (2.046\delta D_X, \delta P_X, \delta H_X)$$
$$D_{SX} = ||P_S - P_X||$$
$$RED_X = D_{SX}/R_X$$

in which $\delta D_X, \delta P_X, \delta H_X$ mean dispersion, polar and H- Bonding, respectively.

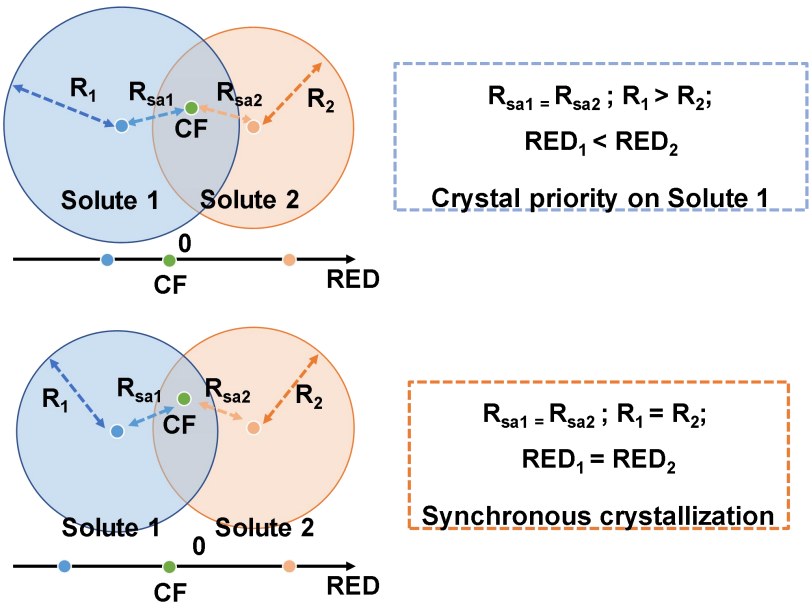

Supplementary Fig. 13. The relationship between RED values difference between two solutes, and corresponding crystallization sequence.

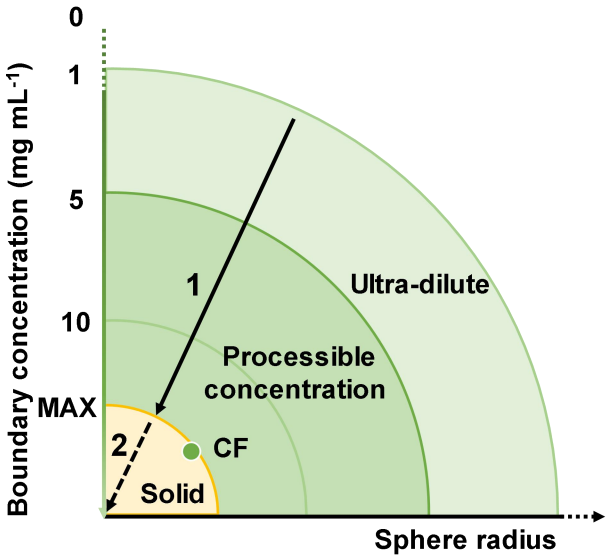

Supplementary Fig. 14. The relationship between solute sphere radius and boundary concentration. The higher the defined boundary concentration, the smaller the radius of the solute sphere. When the boundary concentration is set to 0, all solvents behave as good solvents, causing the radius of the solute sphere to become infinite. **Arrow 1:** During the crystallization process, the concentration of the solution increases steadily, and the radius corresponding to the actual concentration shifts in the direction indicated by the arrows in the figure. **Arrow 2:** the solute sphere's surface reaches chloroform at the corresponding concentration, and the solution concentration reaches saturation concentration, resulting in the formation of a solid phase. At this point, the integration sphere continues to contract inward. In solutions where solid and liquid phases coexist, chloroform acts as a poor solvent.

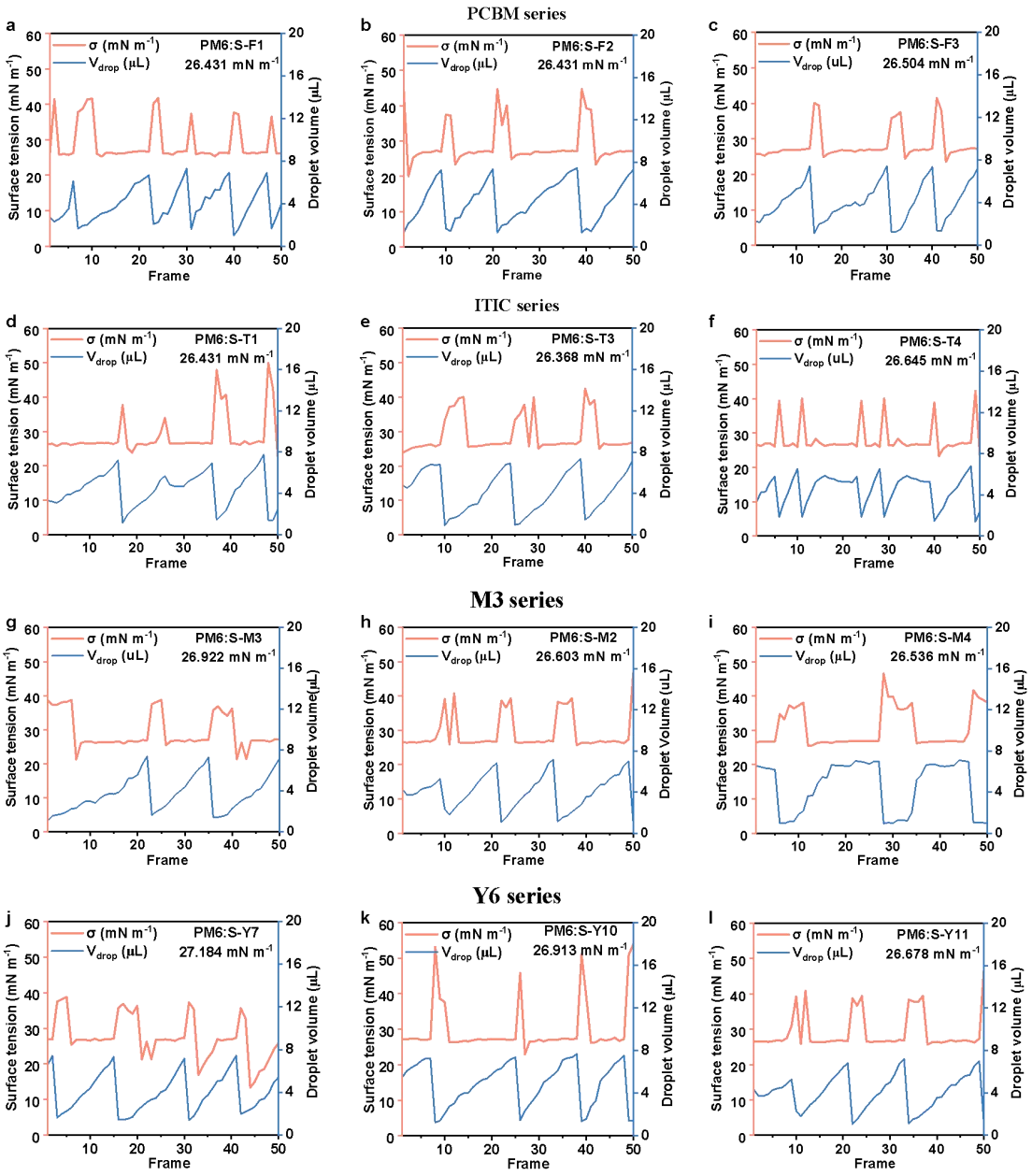

Supplementary Fig. 15. The evolution of the surface tension and droplet volume of PM6: acceptor solutions, the codes of acceptors were (a) S-F1, (b) S-F2, (c) S-F3, (d) S-T1, (e) S-T3, (f) S-F4, (g) S-M2, (h) S-M3, (i) S-M4, (j) S-Y7, (k) S-Y10 and (l) S-Y11, respectively.

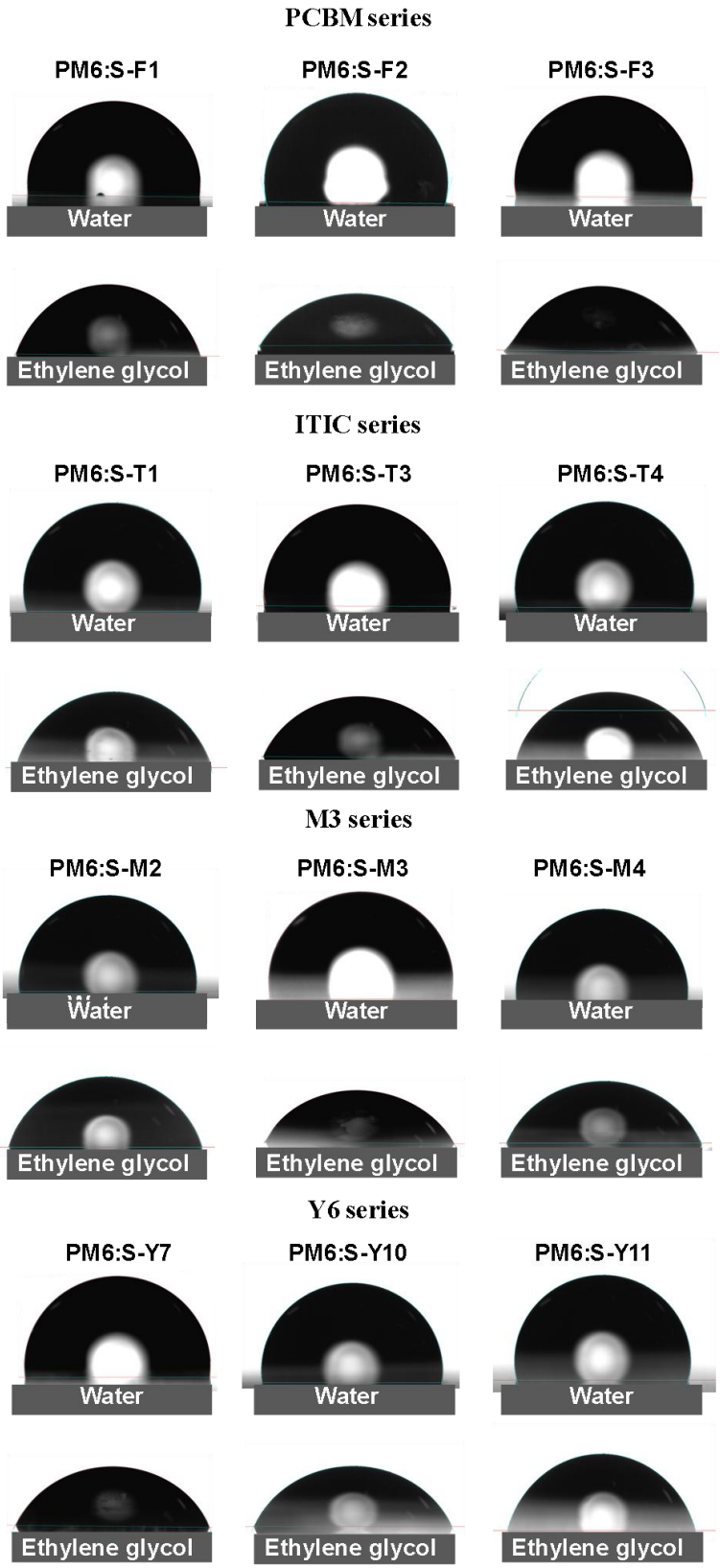

Supplementary Fig. 16. Photographs of deionized water and ethylene glycol droplets on the top surfaces of PM6:S-F1, PM6:S-F2, PM6:S-F3, PM6:S-T1, PM6:S-T3, PM6:S-F4, PM6:S-M2, PM6:S-M3, PM6:S-M4, PM6:S-Y7, PM6:S-Y10, and PM6:S-Y11. The measurement is conducted at the center of the substrates.

Supplementary Table 10. Investigations of the contact angles and surface energy values of solid films of PM6:S-F1, PM6:S-F3, PM6:S-T1, PM6:S-T3, PM6:S-M2, PM6:S-M4, PM6:S-Y10 and PM6:S-Y11.

Sample	Contact angle (°)		Surface energy ($mN\ m^{-1}$)
	Water	Ethylene glycol	
PM6: S-F1	99.82	61.53	27.84
PM6: S-F2	99.51	72.54	27.48
PM6: S-F3	93.29	70.62	22.56
PM6: S-T1	103.53	76.03	31.15
PM6: S-T3	106.03	71.90	30.83
PM6: S-M2	97.30	66.96	36.98
PM6: S-M3	98.34	67.11	34.89
PM6: S-M4	96.10	74.32	35.92
PM6: S-Y7	100.34	67.11	38.74
PM6: S-Y10	98.80	66.30	41.86
PM6: S-Y11	104.23	73.24	38.80

Supplementary Table 11. Summary of surface energy values of solid films and solutions of PM6:S-F1, PM6:S-F3, PM6:S-T1, PM6:S-T3, PM6:S-M2, PM6:S-M4, PM6:S-Y10 and PM6:S-Y11, and corresponding calculated spread force.

Sample	Two-phase Tension (mN m^{-1})		Spread Force (mN m^{-1})
	Solid-Gas	Liquid-Gas	
PM6: S-F1	27.84	26.43	1.41
PM6: S-F2	26.41	27.48	-1.07
PM6: S-F3	22.56	26.50	-3.94
PM6: S-T1	31.15	26.48	4.67
PM6: S-T3	30.83	26.37	4.46
PM6: S-T4	31.56	26.65	4.91
PM6: S-M2	36.98	26.92	10.06
PM6: S-M3	34.89	26.60	8.29
PM6: S-M4	35.92	26.54	9.38
PM6: S-Y7	38.74	27.18	11.56
PM6: S-Y10	41.86	26.91	10.57
PM6: S-Y11	38.80	26.68	12.37

Supplementary Note 3.

Saturation concentration measurement: The saturation concentration of solution can be calculated by analyzing the solution PL intensity as a function of heating-evaporation time.

The solution photoluminescence spectrum intensity can be calculated by:

$$\mathrm{I_{PL}}(\lambda) = \eta_{\mathrm{PL}} \cdot \Phi_{\mathrm{abs}}(\lambda) \cdot \mathrm{I_{exc}}(\lambda) \cdot \mathrm{L} \cdot \mathrm{C}$$

where the η_{PL} is photoluminescence quantum efficiency, representing the probability of emitting one photon per absorbed photon, $\Phi_{\mathrm{abs}}(\lambda)$ is the flux of absorbed photons at wavelength λ, $I_{\mathrm{exc}}(\lambda)$ is the absorbed photon flux can be expressed in terms of the absorbance A(λ), L is the path length of the sample, typically the thickness of the cuvette or sample holder, *C* is the concentration of a solution.

For a series of solutions of different concentrations of the same acceptor mounted in the same size quartz dish, the first four parameters are consistency. We can get the relationship below:

$$I_{\mathrm{PL}}(\lambda) \propto C$$

We can calculate the solution concentration by PL spectrum peak intensity in controlled conditions. Thus, in this measurement, solutions of different acceptors at a concentration of 20 mg $\mathrm{mL^{-1}}$ are prepared, record the PL intensity of solutions is diluted 1000 times, thereby they are placed openly on a hotplate at a temperature of 45 °C to evaporate the solvent and concentrate solution. Every 2 min, remove the solution from the hotplate and still it for 5 minutes, then pipette the upper solution and measure the PL intensity of solutions diluted 1000 times. The test operation above can be terminated after the peak remains stable three times.

Finally, the saturation concentration can be calculated by:

$$C_{sat} = \frac{20 I_{fi}}{I_{in}}$$

Where I_{fi} is the final PL spectrum intensity, I_{in} is the PL spectrum intensity of solution at a concentration of 20 mg mL^{-1}.

***Dynamic pendant drop measurements*:** The pendant drop silhouette images were instantaneously captured, by which the surface tension was calculated with below Young-Laplace equation below in real-time:

$$\gamma = \frac{\Delta \rho g D_e^2}{H},$$

$$\frac{1}{H} = f\frac{D_s}{D_E},$$

Where γ denotes the surface tension of the solution, Δρ denotes the density difference between the solution and air, g represents a gravitational constant, D_e denotes the maximum diameter of the pendant drop, D_s denotes the diameter at the height of D_e, and H represents a shape factor of the pendant drop, which can be calculated with two parameters of D_e and D_s from the images and a correction constant off. To prevent surface crystallization, the solution was continuously and slowly injected into the droplet, the geometry of the threshold volume droplet will stabilize briefly before dropping, corresponding calculated value is the intrinsic surface tension.

All corresponding data in this work were measured under a controlled atmosphere with 25 ℃ and 38% humidity to exclude the air's influence on the evaporation rate.

***Spread force calculation*:** In this study, the spreading force at the three-phase contact point was calculated using the equation:

$$F_{spread} = \sigma_{sg} - \sigma_{ls} - \sigma_{lg} cos\theta$$

Where F_{spread} represents the resultant force of the three interfacial tensions at the three-phase contact point, σ_{sg} is the solid-gas interfacial tension, σ_{ls} is the liquid-solid interfacial tension, and σ_{lg} is the liquid-gas interfacial tension. The variable denotes

the contact angle between the liquid film's edge and the solid phase at the three-phase contact point. Given that the wet film thickness during actual processing is negligible compared to the device size, we assume the contact angle and σ_{ls} , which are approximately 0. Additionally, since the solution near the solid phase interface is close to a semi-solid state, we ensure that the value of σ_{ls} is constant.In this work, we focus on comparing the changes in the resultant force caused by variations in the solid-gas and liquid-gas interfacial tensions:

$$F_s = F_{spread} + \sigma_{ls} = \sigma_{sg} - \sigma_{lg}$$

The surface tension of the solid-gas interface is obtained via contact angle measurements, while the surface tension of the solution-gas interface is measured using the dynamic pendant drop method.

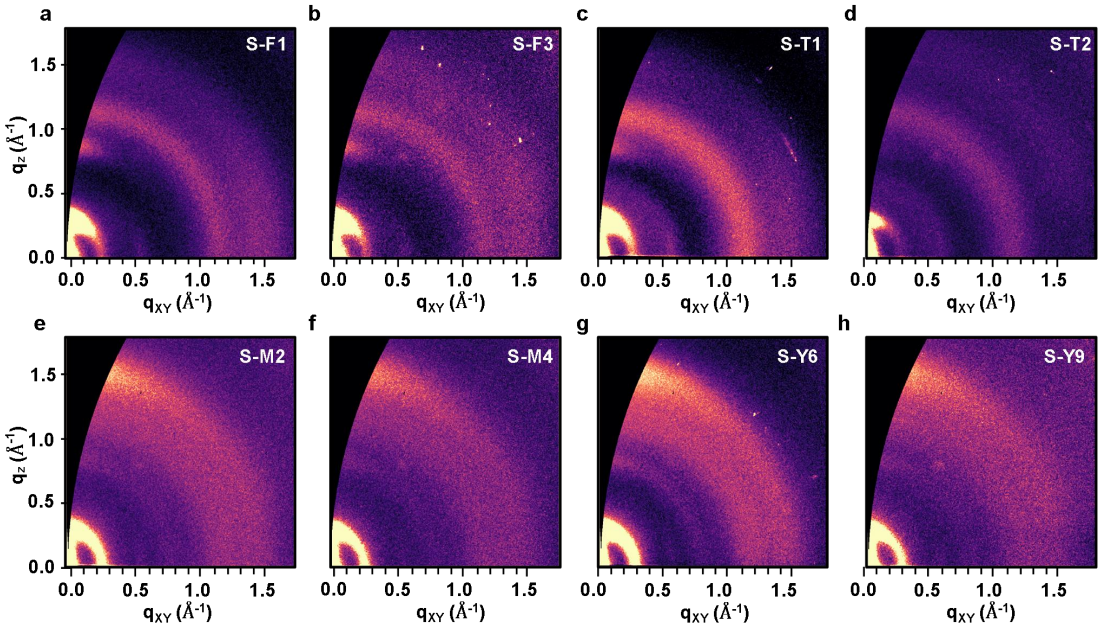

Supplementary Fig. 17. The GIWAXs figures of PM6:(a) S-F1, (b) S-F2, (c) S-T1, (d) S-T2, (e) S-M2, (f) S-M4, (g) S-Y6, (h) S-Y9 film fabricated by low speed.

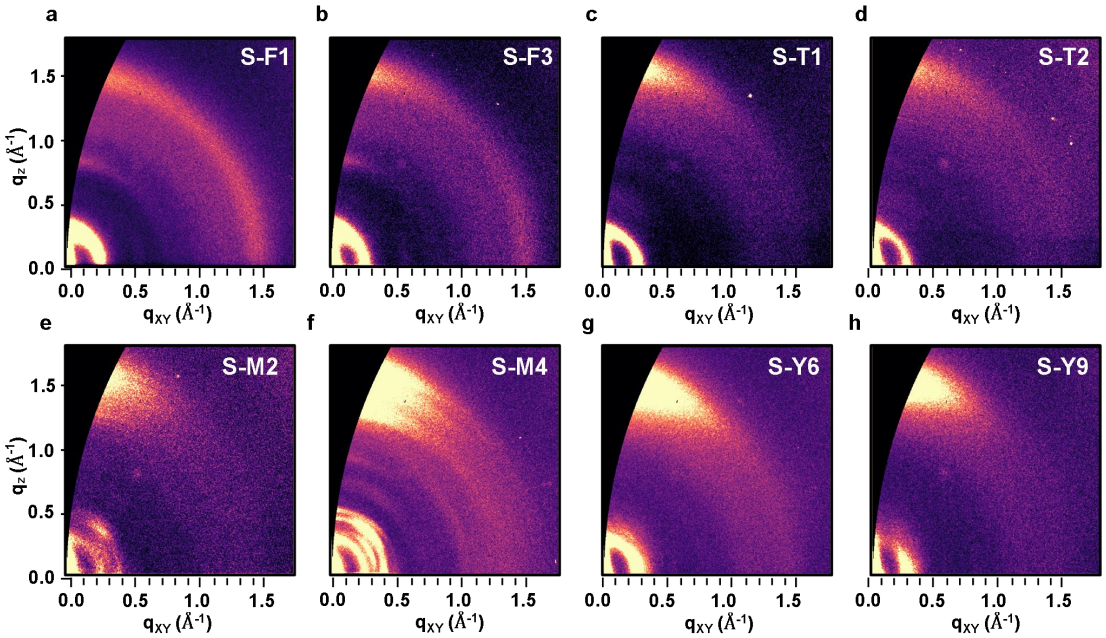

Supplementary Fig. 18. The GIWAXs figures of PM6:(a) S-F1, (b) S-F2, (c) S-T1, (d) S-T2, (e) S-M2, (f) S-M4, (g) S-Y6, (h) S-Y9 film fabricated by low speed.

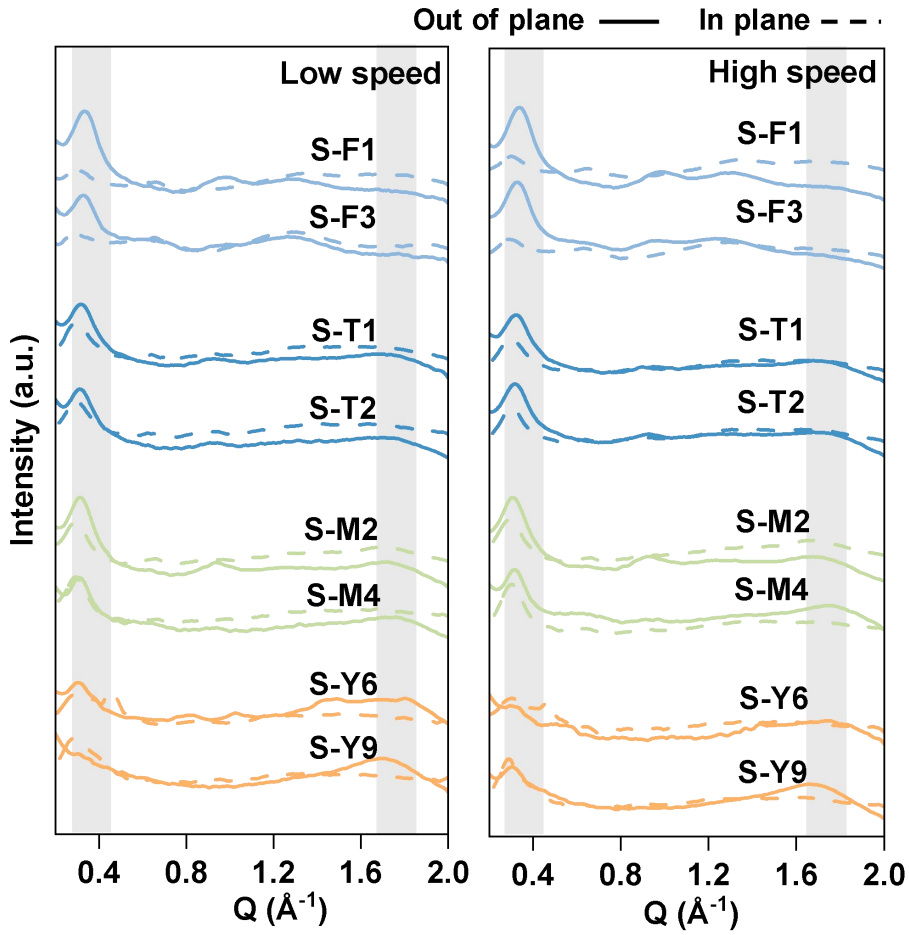

Supplementary Fig. 19. The GIWAXS figures of PM6:S-F1, S-F2, S-T1, S-T2, S-M2, S-M4, S-Y6, S-Y9 film fabricated by low speed and high speed.

Supplementary Table 12. Summarized parameters of PPM6:S-F1, S-F2, S-T1, S-T2, S-M2, S-M4, S-Y6, S-Y9 film fabricated by low speed and high speed. calculated from 1D-GIWAXS scattering profiles

Speed	Sample	Out-of-plane (OOP)				In-plane (IP)	
		q ($Å^{-1}$)	*d*-spacing (Å)	FWHM ($Å^{-1}$]	CCL (nm)	*q* ($Å^{-1}$)	*d*-spacing (Å)
Low	PM6: S-F1	1.292	4.863	0.386	29.230	0.295	21.306
	PM6: S-F3	1.263	4.976	0.365	30.986	0.296	21.198
	PM6: S-T1	1.688	3.723	0.360	31.416	0.302	20.840
	PM6: S-T2	1.690	3.717	0.345	32.782	0.296	21.198
	PM6: S-M2	1.708	3.680	0.290	30.060	0.288	21.786
	PM6: S-M4	1.758	3.575	0.230	39.173	0.293	21.452
	PM6: S-Y6	1.720	3.653	0.325	34.800	0.286	21.977
	PM6: S-Y9	1.695	3.707	0.260	32.500	0.287	21.862
High	PM6: S-F1	1.315	4.778	0.332	29.0651	0.301	20.909
	PM6: S-F3	1.238	5.077	0.420	26.928	0.290	21.636
	PM6: S-T1	1.698	3.701	0.295	36.338	0.298	21.092
	PM6: S-T2	1.688	3.723	0.335	33.760	0.302	20.778
	PM6: S-M2	1.683	3.734	0.290	39.000	0.291	21.562
	PM6: S-M4	1.758	3.575	0.245	46.162	0.301	20.847
	PM6: S-Y6	1.740	3.611	0.270	41.888	0.304	20.641
	PM6: S-Y9	1.665	3.773	0.275	41.126	0.288	21.786

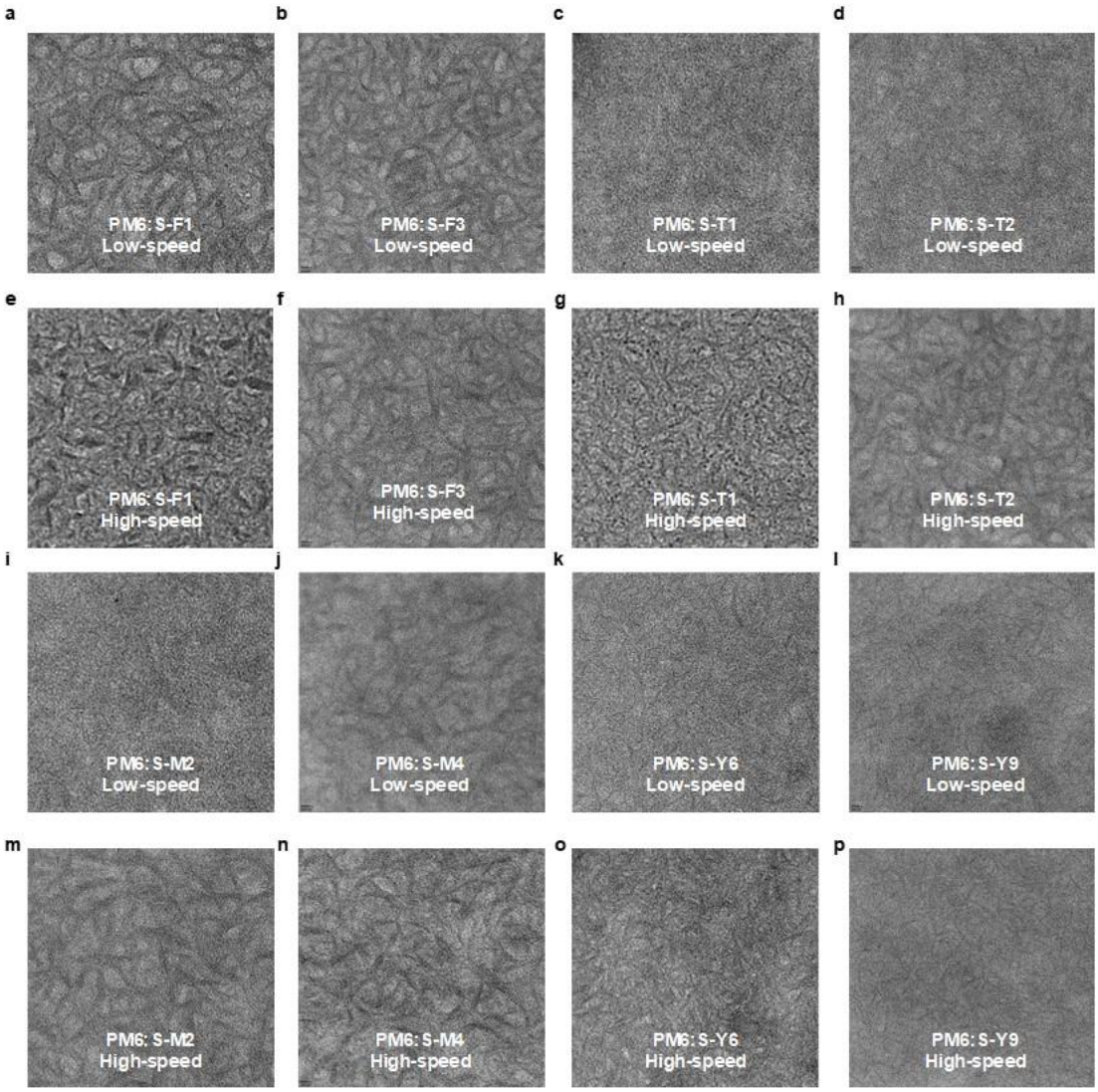

Supplementary Fig. 17. The TEM figures of PM6:(a) S-F1, (b) S-F2, (c) S-T1, (d) S-T2, (e) S-M2, (f) S-M4, (g) S-Y6, (h) S-Y9 film fabricated by low speed and the figures of PM6:(i) S-F1, (j) S-F2, (k) S-T1, (l) S-T2, (m) S-M2, (n) S-M4, (o) S-Y6, (p) S-Y9 film fabricated by high speed.

References

1 Brabec, C. J. *et al.* Production Aspects of Organic Photovoltaics and Their Impact on the Commercialization of Devices. *MRS Bull.* **30**, 50-52 (2005).

2 Liang, Y. *et al.* For the Bright Future—Bulk Heterojunction Polymer Solar Cells with Power Conversion Efficiency of 7.4%. *Adv. Mater.* **22**, E135-E138 (2010).

3 Zhao, G. *et al.* 6.5% Efficiency of Polymer Solar Cells Based on poly(3-hexylthiophene) and Indene-C60 Bisadduct by Device Optimization. *Adv. Mater.* **22**, 4355-4358 (2010).

4 Zhao, W. *et al.* Molecular Optimization Enables over 13% Efficiency in Organic Solar Cells. *J. Am. Chem. Soc.* **139**, 7148-7151 (2017).

5 Lin, Y. *et al.* An electron acceptor challenging fullerenes for efficient polymer solar cells. *Adv. Mater.* **27**, 1170-1174 (2015).

6 Ali, A. *et al.* Evaluating the impact of Hartree–Fock exact exchange on the performance of global hybrid functionals for the vertical excited-state energies of fused-ring electron acceptors using TD-DFT. *Phys. Chem. Chem. Phys.* **24**, 21270-21282 (2022).

7 Liu, Y. *et al.* Enhancing the Performance of Non-Fullerene Organic Solar Cells Using Regioregular Wide-Bandgap Polymers. *Macromolecules* **51**, 8646-8651 (2018).

8 Ma, Y. *et al.* Efficient Organic Solar Cells from Molecular Orientation Control of M-Series Acceptors. *Joule* **5**, 197-209 (2021).

9 Ma, Y. *et al.* 17% efficiency for linear-shaped ADA-type nonfullerene acceptors enabled by 3D reticulated molecular packing. *Nano Energy* **107**, 108116 (2023).

10 Tang, C. *et al.* High-Performance Ladder-Type Heteroheptacene-Based Nonfullerene Acceptors Enabled by Asymmetric Cores with Enhanced Noncovalent Intramolecular Interactions. *Angew. Chem. Int. Ed.* **60**, 19314-19323 (2021).

11 Yuan, J. *et al.* Single-Junction Organic Solar Cell with over 15% Efficiency Using Fused-Ring Acceptor with Electron-Deficient Core. *Joule* **3**, 1140-1151 (2019).

12 Cui, Y. *et al.* Single-Junction Organic Photovoltaic Cells with Approaching 18% Efficiency. *Adv. Mater.* **32**, 1908205 (2020).

13 Li, C. *et al.* Non-fullerene acceptors with branched side chains and improved molecular packing to exceed 18% efficiency in organic solar cells. *Nat. Energy* **6**, 605-613 (2021).

14 Chen, Y. *et al.* Alkoxy substitution on IDT-Series and Y-Series non-fullerene acceptors yielding highly efficient organic solar cells. *J. Mater. Chem. A* **9**, 7481-7490 (2021).

15 Hong, L. *et al.* Eco-Compatible Solvent-Processed Organic Photovoltaic Cells with Over 16% Efficiency. *Adv. Mater.* **31**, 1903441 (2019).

16 Zhu, Y. *et al.* Exciton Binding Energy of Non-Fullerene Electron Acceptors. *Adv. Energy Sustain. Res.* **3**, 2100184 (2022).

17 Sun, R. *et al.* Single-Junction Organic Solar Cells with 19.17% Efficiency Enabled by Introducing One Asymmetric Guest Acceptor. *Adv. Mater.* **34**, 2110147 (2022).

18 Zhan, L. *et al.* Layer-by-Layer Processed Ternary Organic Photovoltaics with Efficiency over 18%. *Adv. Mater.* **33**, 2007231 (2021).

19 Yin, B. *et al.* A structurally simple linear conjugated polymer toward practical application of organic solar cells. *Energ. Environ. Sci.* **15**, 4789-4797 (2022).

20 Dong, S. *et al.* Single-Component Non-halogen Solvent-Processed High-Performance Organic Solar Cell Module with Efficiency over 14%. *Joule* **4**, 2004-2016 (2020).

21 Moustafa, E. *et al.* Thermal Activation of PEDOT:PSS/PM6:Y7 Based Films Leads to Unprecedent High Short-Circuit Current Density in Nonfullerene Organic Photovoltaics. *Adv. Energy Mater.* **13**, 2203241 (2023).

22 Liu, W. *et al.* A-π-A structured non-fullerene acceptors for stable organic solar cells with efficiency over 17%. *Sci. China Chem.* **65**, 1374-1382 (2022).

23 Machui, F. *et al.* Determination of the P3HT:PCBM solubility parameters via a binary solvent gradient method: Impact of solubility on the photovoltaic performance. *Sol. Energy Mater. Sol. Cells* **100**, 138-146 (2012).